

Growth of pellet imperfections and laser imprint in direct drive inertial confinement fusion targets

Andrew J. Schmitt, A. L. Velikovich, J.H. Gardner*, C. Pawley, S.P. Obenschain

Plasma Physics Division, Naval Research Laboratory, Washington DC 20375

Y. Aglitskiy, Y. Chan

Science Applications International Corp., McLean Virginia 22102

Abstract

Simple hydrodynamic models for describing the Richtmyer-Meshkov (RM) growth and the Rayleigh-Taylor (RT) instability are tested by simulation. The RM sharp boundary model predictions are compared with numerical simulations of targets with surface perturbations or stationary intensity perturbations. Agreement is found in the overall trends, but the specific behavior can be significantly different. RM growth of imprint from optically smoothed lasers is also simulated and quantified. The results are used to calculate surface perturbations, growth factors, and laser imprint efficiencies. These in turn are used with standard RT growth formulas to predict perturbation growth in multimode simulations of compression and acceleration of planar and spherical targets. The largest differences between prediction and theory occur during ramp-up of the laser intensity, where RT formulas predict more growth than seen in the simulations.

52.57.Fg, 47.40.nm

Typeset using REVTeX

*at the Laboratory for Computational Physics & Fluid Dynamics

Report Documentation Page

Form Approved
OMB No. 0704-0188

Public reporting burden for the collection of information is estimated to average 1 hour per response, including the time for reviewing instructions, searching existing data sources, gathering and maintaining the data needed, and completing and reviewing the collection of information. Send comments regarding this burden estimate or any other aspect of this collection of information, including suggestions for reducing this burden, to Washington Headquarters Services, Directorate for Information Operations and Reports, 1215 Jefferson Davis Highway, Suite 1204, Arlington VA 22202-4302. Respondents should be aware that notwithstanding any other provision of law, no person shall be subject to a penalty for failing to comply with a collection of information if it does not display a currently valid OMB control number.

1. REPORT DATE 2001	2. REPORT TYPE	3. DATES COVERED 00-00-2001 to 00-00-2001			
4. TITLE AND SUBTITLE Growth of pellet imperfections and laser imprint in direct drive inertial confinement fusion targets		5a. CONTRACT NUMBER			
		5b. GRANT NUMBER			
		5c. PROGRAM ELEMENT NUMBER			
6. AUTHOR(S)		5d. PROJECT NUMBER			
		5e. TASK NUMBER			
		5f. WORK UNIT NUMBER			
7. PERFORMING ORGANIZATION NAME(S) AND ADDRESS(ES) Naval Research Laboratory, Plasma Physics Division, 4555 Overlook Avenue SW, Washington, DC, 20375		8. PERFORMING ORGANIZATION REPORT NUMBER			
9. SPONSORING/MONITORING AGENCY NAME(S) AND ADDRESS(ES)		10. SPONSOR/MONITOR'S ACRONYM(S)			
		11. SPONSOR/MONITOR'S REPORT NUMBER(S)			
12. DISTRIBUTION/AVAILABILITY STATEMENT Approved for public release; distribution unlimited					
13. SUPPLEMENTARY NOTES This article appeared in Physics of Plasmas and may be found at Phys. Plasmas 8, 2287 (2001)					
14. ABSTRACT Simple hydrodynamic models for describing the Richtmyer-Meshkov (RM) growth and the Rayleigh-Taylor (RT) instability are tested by simulation. The RM sharp boundary model predictions are compared with numerical simulations of targets with surface perturbations or stationary intensity perturbations. Agreement is found in the overall trends, but the specific behavior can be significantly different. RM growth of imprint from optically smoothed lasers is also simulated and quantified. The results are used to calculate surface perturbations, growth factors, and laser imprint efficiencies. These in turn are used with standard RT growth formulas to predict perturbation growth in multimode simulations of compression and acceleration of planar and spherical targets. The largest differences between prediction and theory occur during ramp-up of the laser intensity, where RT formulas predict more growth than seen in the simulations.					
15. SUBJECT TERMS					
16. SECURITY CLASSIFICATION OF:			17. LIMITATION OF ABSTRACT	18. NUMBER OF PAGES	19a. NAME OF RESPONSIBLE PERSON
a. REPORT unclassified	b. ABSTRACT unclassified	c. THIS PAGE unclassified	Same as Report (SAR)	31	

I. INTRODUCTION

Because of the wide scope and complexity of the physics involved, inertial confinement fusion (ICF) targets are traditionally designed with elaborate radiation hydrodynamic codes. The intent is to create a target that is highly compressed yet resistant to hydrodynamic instabilities. The first criterion can easily be satisfied using a one-dimensional (1D) hydrocode, but the analysis of hydrodynamic instability requires two-dimensional (2D) and/or three-dimensional (3D) codes to simulate. For many years, we have had available simple growth formulas for the Rayleigh-Taylor (RT) growth of instabilities, with some indication that they were fairly accurate in describing the growth seen in both simulations and experiments [1–4]. These formulas can be applied to the acceleration stage of the target drive, but not to the earlier stage during which the target is being compressed. In recent years however, new Richtmyer-Meshkov (RM) models and theory have been developed that can describe the formation and evolution of perturbations during the compression [5–9]. With these recently developed RM models, the potential now exists to describe the hydrodynamic instability growth from start to finish by using a 1D hydrocode, extracting the relevant parameters for use in the models, and predicting the 2D or 3D instability levels. This paper addresses the question of whether or not this is a fruitful exercise.

First, we use the Richtmyer-Meshkov theory to describe the evolution of surface perturbations or stationary laser imprint during target compression. Analysis of surface perturbation growth provides us with a growth factor, defined as the ratio of the perturbation amplitude at the end of imprint to the initial amplitude. Imprint analysis gives us an “imprint efficiency” which allows us to calculate the equivalent surface finish induced by stationary laser nonuniformity, and thus the corresponding end-of-imprint perturbation. We compare the results of this theoretical model to simulation results.

Unfortunately, current laser drivers in ICF applications are optically smoothed, and so are not stationary but inherently time-dependent. This temporary inconvenience is overcome by allowing our FAST2D hydrocode [10] to simulate the problem and provide a numerically

generated imprint efficiency for optically smoothed light.

The Richtmyer-Meshkov phase ends when the laser intensity begins to increase and the ablation surface begins to accelerate. About this same time, the possibility of feedout becomes important. Feedout theory describes the development of rear surface perturbations that propagate to the ablation surface. Very recent analytic results [11] can be used to quantify this contribution. Feedout ends when the rarefaction wave from the rear surface arrives at the front-side ablation surface.

As the Richtmyer-Meshkov phase ends, we turn to the Rayleigh-Taylor growth formulas to provide our predictions. These use as their seed the perturbations that have been generated during RM. We use a variety of dispersion relations to describe this growth, from simple models to more sophisticated ones. For the target we use here (in the large Froude number limit) all the formulas give very similar results. We also compare these formulas to the simulation results.

This modeling and comparison will be done in the context of describing a relatively simple target, shown in Fig. 1. This is the directly-driven pure DT spherical target initially developed by Verdon [3,12] for the National Ignition Facility (NIF). It is composed of a spherical shell of DT ice covered by a thin (few microns thick) outer membrane of plastic (which we will ignore here). The DT serves both as the the ablator and the fuel for the burn. Other directly-driven designs differ mainly in the ablator constituency, the pellet aspect ratio (the radius normalized to the shell thickness) and the specifics of the drive laser pulse; however, all ICF target designs share the same basic imprint-and-instability physics we discuss here. This NIF target is driven by a laser pulse with a relatively constant foot (10 TW) followed by a rapid rise to a constant main pulse (~ 450 TW). The foot serves to compress the pellet shell and ready the target for acceleration. When the target is nearly compressed, the laser intensity rapidly rises to its main power level where acceleration and Rayleigh-Taylor begins.

We find that the largest discrepancy between the simple models and the behavior observed in the simulation occurs during the transition between the RM and RT growth. While

the observed perturbations grow somewhat during this time, the growth is significantly less than predicted. There are also smaller discrepancies between the models and simulation during the RM phase, but this can be ascribed to deviations from the idealized assumptions of the RM model.

II. RICHTMYER-MESHKOV PHASE

The ‘sharp boundary model’ (SBM) of Richtmyer-Meshkov growth [13,8,9] is used to describe the evolution of the initially small amplitude perturbations during the compression of the target. This model uses an undriven acoustic wave equation to describe the fluid between the ablation and shock front surfaces. Much of the physics is concentrated in the boundary conditions of this equation, which include Rankine-Hugoniot jump conditions at the shock front, mass and momentum continuity at the ablation surface, and an isothermal ablation front. In addition, intensity perturbations are assumed to be smoothed thermally ($\sim \exp(-kd)$) over the distance between the ablation and absorption surfaces. The parameters needed for this model are the pellet density and γ (ratio of specific heats), shock pressure (7 Mbar), ablation velocity ($V_{abl} = 2 \times 10^5$), density scalelength at the ablation surface ($L_{min} = 0.3\mu\text{m}$), and the temperature exponent of thermal conduction (we use $\nu = 2$ instead of Spitzer’s 5/2 [4]). In addition, the coronal blow-off velocity is needed when calculating imprint from intensity perturbations. These derived parameters all exhibit some time dependence during the RM phase in the simulations (for instance, due to the laser decoupling from the ablation surface), so the values quoted here are appropriate time averages.

A. Surface finish imperfections

A priori surface imperfections on the target form a primary contribution to RT seeding. Outer surface perturbations are most important since they have the most time to grow before acceleration begins. We have performed many single mode calculations of these

surface perturbations in planar geometry to test the agreement with the basic theory. Planar geometry is used because the RM theory was developed with this assumption; it is expected to accurately model the spherical pellet during the imprint time as no significant convergence effects take place during this stage.

Theoretical predictions and simulation results for the DT target are shown in Fig. 2 for various perturbation wavelengths. The same general behavior is seen in both the simulation and theory: an initial increase in amplitude to a saturation point and the approximate time to phase reversal are reproduced by both methods. (Phase reversal is the time at which the areal mass perturbation passes through zero and becomes negative with respect to the perturbation before. Thick target regions become thinner regions and vice-versa). After about 4 ns, the simulation behavior diverges as the laser pulse in these simulations begins to rise towards full power; current Richtmyer-Meshkov theory is unable to handle this situation. RT theory is more applicable in this case because the ablation surface begins to accelerate.

At the later times, evolution at smaller wavelengths is oscillatory. Although the mass perturbation can temporarily become zero as it passes through a phase reversal, the perturbation energy and momentum are quite finite. For instance, the SBM model predicts that the perturbed kinetic energy is fairly constant during this period. In light of this behavior, we (somewhat arbitrarily) define the imprint measure as the maximum value of the induced areal mass between the times of 2-4 nsec. We believe that this measure will provide a reasonable assessment of the true perturbation level then.

Using this metric, we define a growth factor, given by the perturbation amplitude at the end of the imprint phase divided by its initial amplitude. As the response during this stage is linear, this growth factor allows one to predict the RT seed due to arbitrary surface perturbations. Fig. 3 shows that the theory and the simulations agree that growth for wavelengths larger than $100 \mu\text{m}$ decreases with wavelength in a similar manner. At shorter wavelengths, however, the simple model predicts growth independent of wavelength while the simulations show a peak near $50 \mu\text{m}$ and a fall-off for smaller wavelengths. We will use the numerically generated growth factor for further comparisons in the following sections.

B. Laser beam imprint

Important contributions to the RT seeding also come from perturbations that develop due to spatial imperfections of the driving pulse, which is customarily known as ‘imprint’. In most ICF scenarios today, this imprint is due to residual nonuniformities from an optically smoothed laser that uses a spatially varying intensity profile which changes completely on the laser coherence time scale, t_c (typically a picosecond). While the instantaneous intensity distribution is very rough, the average over times much larger than the laser coherence time is much smoother, with perturbations decreasing as $\sqrt{t_c/t}$.

We address laser imprint here as a two part problem. First, we calculate the imprint due to stationary intensity perturbations. This includes the physics of how the laser light is converted to pressure perturbations and how those pressure perturbations are transported to the ablation surface and beyond. Stationary imprint can in principle be described straightforwardly by the SBM, so we can compare theory and simulation. Secondly, we consider the effect of optically smoothing the laser, which current SBM models do not address.

1. Stationary imprint

We first run the simulations for many instances of single mode intensity perturbations. The perturbation wavelength is varied in the range of 100 μm while its amplitude is held constant at 1% of the average intensity. An additional parameter that describes the absorption-to-ablation distance (and accounts for the coronal thermal smoothing) is needed for the theory. Following convention, we choose the rate at which this absorption-to-ablation distance increases to be determined by the blow-off velocity V_b in the underdense plasma. Since the blow-off velocity in an actual plasma increases with the distance from the ablation surface, we use the standard prescription [13] that $V_b = r_D(\lambda)V_a$. $r_D(\lambda)$ is the ratio of the ablation density to the blow-off density a distance λ away from the ablation surface. As the absorption region convects away from the ablation surface with this blow-off velocity,

the pressure perturbation at the ablation surface decays as $\exp(-kV_b t)$. (We have used an alternative prescription of a constant V_b [$\simeq 2 \times 10^6 \text{ cm/s}$], but this results in a longer decoupling time at longer wavelengths and a worse match with simulation). The theoretical results are compared to the simulation in Fig. 4; differences between the simulation and theory are again most significant in the wavelength range less than $200\mu\text{m}$. In contrast to the surface imprint case, the shorter wavelength simulation imprint stabilizes and reverses phase earlier than the theoretical prediction. At longer wavelengths, the simulation growth appears to be slower than theory. We believe that the simulation behavior implies that the physics involved in intensity driven imprint is more complex than the simple model allows, with its approximation of a constantly increasing separation distance combined with thermal smoothing.

Imprint can also be equated to surface perturbations using the concept of ‘imprint efficiency’ [3]. The imprint efficiency is the amplitude of initial surface perturbation that would give rise to the same perturbed mass as an intensity perturbation of 100%:

$$E(\lambda) = \frac{\delta m_I(\lambda, \delta I/I_0)}{\delta m_s(\lambda, a_0)} \frac{a_0}{\delta I/I_0} \quad (1)$$

where a_0 is the initial surface perturbation amplitude and $\delta I/I_0$ is the normalized intensity perturbation amplitude. The results (Fig. 4) show that a 1% intensity variation is equivalent to $\simeq 1.6\mu\text{m}$ surface finish ($0.4 \text{ gm} - \mu\text{m}/\text{cm}^3$) at $\sim 200\mu\text{m}$, with smaller values for larger or smaller wavelengths. It peaks at about $\sim 200\mu\text{m}$ because perturbations of this wavelength tend to reach their first point of saturation when this measurement is taken (2-4 ns); shorter wavelengths saturate and begin to decay before this time, while longer wavelengths have not yet grown to the point of saturation.

The observed imprint decrease for long wavelengths is dependent on the imprint metric used. At large wavelengths and fixed imprint time, the mass redistribution responsible for the imprint observed here goes to zero as $\sim c_s t_{\text{imprint}}/\lambda$. In contrast, if surface perturbation amplitude (e.g., ablation surface contour) is used to measure imprint, the response at long wavelengths to steady laser perturbations tends to a finite constant amplitude, which is larger

than the response at smaller wavelengths. This asymptotic behavior is due to the ablation and shock fronts moving at different local velocities due to the (local) pressures associated with the intensity perturbation. There is little time for mass redistribution to occur, and the perturbations will have a "ribbon-like" structure with the ablation front and shock front perturbation in phase. We find this asymptotic behavior occurring here at wavelengths greater than about $200 \mu m$. During the later Rayleigh-Taylor stage, these ribbon distortions will grow by mass redistribution and result in detectable areal mass variations. We do not find such surface perturbations without mass perturbation for optically smoothed imprint, since the front and rear surfaces are not in phase with each other even at long wavelengths; in this case both surface and areal mass perturbations decrease as the wavelength increases.

2. Optically smoothed imprint

Next we calculate the evolution of perturbations due to optically smoothed light. This light is defined by its bandwidth ($\Delta\nu \sim 1/t_c$), spatial coherence, lens f-number ($f/\#$), and laser wavelength. Its spatial structure encompasses a wide range of wavelengths, with the mean intensity amplitude at a given wavelength determined by the $f/\#$ and spatial coherence. We begin to study this in the simplest manner by performing simulations of single mode incoherent fluctuations. Our incoherence model selects a single mode out of our standard induced-spatial-incoherence (ISI) model [14]. Here, the amplitude of any mode has a random Gaussian-shaped probability distribution and a uniform random phase (with respect to the transverse coordinate and time). Both of these parameters change discretely and randomly at each coherence time. This produces an intensity that smooths with time as $\sqrt{t_c/t}$, like the ISI and smoothing-by-spectral-dispersion (SSD) optical smoothing methods. ISI and SSD are sufficiently alike in their incoherence properties that this model will sufficiently describe either.

Full raytracing is not used for the optical smoothing simulations here because of concerns with the fluctuations in the resulting energy deposition competing with the statistical

fluctuations due to the laser light incoherence. Instead we use a hybrid 1D/2D model that raytraces the light along the axial (x direction) density variation at each transverse y coordinate separately, ignoring transverse density gradients (except those associated with the geometry). This method correctly accounts for the increased standoff of the laser absorption from the critical surface due to oblique ray propagation, but not for potential refraction effects due to local transverse density gradients.

With the preceding incoherence model, the spectrum of intensity perturbations at the target plane has a mean value [14]:

$$\langle I(\kappa) \rangle = \sqrt{\frac{1 - \kappa \pi}{N_z} \frac{\pi}{4}} I_{avg} \quad (2)$$

where $\kappa = |k|/k_{max}$, $N_z = k_{max} D_{spot}/2\pi$, $k_{max} = 2\pi/f\lambda_0$, λ_0 is the laser wavelength, D_{spot} is the laser spot diameter, and $k \neq 0$. This spectrum is a 1D spectrum (i.e., from a cylindrical lens) and is appropriate for 2D simulations that only describe one transverse dimension. The analogous spectrum for two transverse dimensions due to a circular lens is:

$$\langle I(\kappa) \rangle = \sqrt{\pi - 2 \sin^{-1}[\kappa] - 2\kappa\sqrt{1 - \kappa^2}} \frac{I_{avg}}{2N_z} \quad (3)$$

where $\kappa = \sqrt{\kappa_x^2 + \kappa_y^2}$. This is similar in shape to the 1D spectrum, but the mean fluctuation level of any mode is smaller by $\sim \sqrt{N_z}$. When summed over the surface of a plane however, the total σ_{rms} of the 2D spectrum is identical to the 1D spectrum summed over the single dimension. In both 1D & 2D, these formulas are reduced by $\sqrt{2}$ when polarization smoothing is used and by $\sqrt{N_b}$ when N_b beams are overlapped on the target.

Because of the random statistical nature of incoherence, single mode calculations of optically smoothed light must be performed many times in order to yield an average expected value for smoothing. For example, we have simulated single modes of optically smoothed light while varying the perturbation wavelength from 25 μm to 800 μm . To get a sense of the run-to-run variation, we repeated the calculations five times each, and recorded the response from each group of five runs. As Fig. 5 shows, the results show a scatter that can vary by as much as a factor of five. Averaging these results and accounting for the intensity

fluctuation level in these simulations gives the optically smoothed imprint efficiency. Like stationary intensity imprint, it is defined by equating a 100% mean (instantaneous) intensity fluctuation with a surface perturbation yielding the same response. This quantity is shown in Fig. 5(b) as a function of the perturbation wavelength. The largest response is once again found near $\sim 200\mu\text{m}$, due to the same considerations responsible for the similar peak in stationary imprint.

Consider the implications of this imprint efficiency for the pure-DT pellet. Assuming a spot size = 0.338 cm (the DT pellet diameter), f/30 optics, 32 beam overlap, and the use of polarization smoothing at 1.0 THz laser bandwidth, the intensity distribution is determined using Eq. (2) or (3) above. Multiplying this spectrum by the imprint efficiency gives the equivalent surface finish spectrum. Summing over all ℓ modes, this yields the prediction that the total σ_{rms} for the equivalent surface finish over the DT pellet surface due only to this optical smoothing is $\simeq 800\text{\AA}$ for the 1D spectra and $\simeq 840\text{\AA}$ for the wavenumber-averaged 2D spectrum. This contrasts with an earlier study [3] which predicts an rms surface finish modulation from imprint to be 110\AA .

One other interesting parameter that can be derived from these results is an implied smoothing time. This smoothing time is found by assuming that the plasma response to the incoherent light is the response to the random instantaneous intensity perturbations averaged over a time t_{smooth} :

$$\frac{\delta m_{smooth}(k, t)}{\delta m_{steady}} \equiv \frac{\delta I/I_{smooth}}{\delta I/I_{steady}} \sqrt{\frac{t_c}{t_{smooth}}} \quad (4)$$

This implied smoothing time is shown in Fig. 6, where it is compared to an acoustic smoothing time $t_a \sim \lambda/c_s$ scaling (c_s is the sound speed). Acoustic scaling assumes that the response at a given wavelength is proportional to the fluctuation level averaged over the hydrodynamic response time of that wavelength. The scaling here does not appear to be that simple.

III. FEEDOUT

There is an additional contribution to the imprint due to transport of perturbations on the target rear surface to the front ablation surface. This process, called feedout, begins when the first shock breaks out of the target and ends when the resulting rarefaction wave arrives at the ablation surface. Earlier theoretical work addressed the long-wavelength limit of feedout [15], but a recent analysis [11] of this process for arbitrary perturbation wavelengths has found a closed form solution for the growth factor, defined as the mass modulation on the ablation surface at the end of feedout divided by the mass modulation on the target's rear surface at the beginning of feedout, for a target of initial thickness L_0 and perturbation wavelength λ :

$$\begin{aligned} \delta m(L_0/\lambda)/\delta m_0(\lambda) = & \\ & \frac{2(3-\gamma)(\gamma+1)}{\gamma+1-(\gamma-1)\beta} \sum_{j=0}^{\infty} \frac{(-1)^j}{j!} \left[\frac{1}{4} \left(\frac{\gamma+1}{3-\gamma} \right) \left(2\pi \left(\frac{\gamma-1}{\gamma+1} \right) \frac{L_0}{\lambda} \right)^2 \right]^j \frac{\Gamma \left[\frac{2(\gamma-1)}{3-\gamma} j + \frac{3}{2} \right]}{\Gamma \left[\frac{\gamma+1}{3-\gamma} j + \frac{1}{2} \right]} \\ & \times \frac{(\gamma-1)(2j-\beta) + \gamma + 1}{[(\gamma-1)j + 1] \{4[(\gamma-1)j + 1]^2 - (\gamma-1)^2\}} \end{aligned} \quad (5)$$

where

$$\beta = \frac{2\gamma(\gamma+1)}{2\gamma(\gamma-1) + (2\gamma)^{1/2}(\gamma-1)^{3/2}}.$$

The mass modulation at the beginning of feedout is due to surface perturbations that are on the rear of the target when shock breakout occurs. The spectrum of this growth is shown in Fig. 7 for $\gamma=5/3$. The largest growth is about a factor of 4 occurring at the wavelength $\lambda = L_0/6$ (about 60 μm for the DT-ice target). The resulting perturbation from feedout will add linearly to the front-side perturbations considered earlier.

The simulations presented here did not include initial rear surface perturbations, so the only feedout source for these simulations is due to the structured shock interface from the front surface. By the time the shock front reaches the rear surface, its perturbation is typically much smaller than the ablation front perturbation (except for the largest wavelengths,

$\lambda \geq 500\mu\text{m}$ which have minimal growth factors). In addition, the laser intensity is beginning to increase and accelerate the ablation surface even before the shock breaks out the target rear surface, so the ablation front perturbations are already susceptible to significant RT growth before feedout can occur. For these reasons, we will not consider feedout contributions in the results here, except to note that it can be appreciable and is quantifiable in general.

IV. MULTIMODE SIMULATIONS AND RAYLEIGH-TAYLOR GROWTH

Now consider calculations of the entire compression and acceleration of the target, for which the Rayleigh-Taylor instability becomes important. Because RT can quickly become nonlinear, we use multimode calculations that allow the different modes to interact. First we present planar simulations of the imprint and acceleration phase in the planar version of the DT-ice target; then we show simulations of the spherical pellet. Finally we compare the simulations to experimental results.

We remark here that our use of areal mass perturbations ($\int \rho dr$) as an instability measure in this paper is a departure from the customary practice of focusing only on the front surface perturbation. To be sure, the classic analysis of the RT instability shows the growing mode peaked at the front surface. However, most experimental measurements as well as the figure of merit in an imploding ICF pellet involves the mass density integrated through the direction of movement. Furthermore, any mass nonuniformity inside or at the rear of the accelerated shell will soon show up at the front surface (see the discussion of feedout). Finally, use of integrated mass can account correctly for the case where the shell density varies with time, bypassing the complication that a uniformly compressed perturbation amplitude will vary inversely with the local density.

Two specific all-DT target simulations in planar geometry were performed: one begins with a 500\AA randomly rough surface driven by a perfectly uniform laser and the other with a perfectly uniform target driven by a single 0.5 THz optically smoothed laser beam

with polarization smoothing. These were multimode calculations but with a limited number of modes: simulations were 200 μm wide with 128 transverse points, so that modes from 25 μm - 200 μm were resolved with at least 16 points per mode (our criterion for adequate resolution). The black curves on the plots in Fig. 8 show individual modes taken from the multimode calculations. The characteristic growth and oscillation of the imprint phase is clearly seen, as it was in Fig. 2. At about 4 ns, when the laser intensity begins to increase, the modes slowly begin to grow exponentially, but only after a time delay of a nsec or more. The Rayleigh-Taylor instability then clearly takes over until about 7 nsec, when the modes begin to saturate and turn over. At this time, the target begins to decompress rapidly, as there is no spherical convergence to maintain compression.

Also shown on these figures is the predicted mode level using the simulated growth factor (Fig. 3) and the RT dispersion relation used by Weber [3]:

$$\gamma = \sqrt{kg/(1 + kL)} - 3kV_a \quad (6)$$

The values of acceleration (g), ablation density scalelength (L), and ablation velocity (V_a) used in this formula are time dependent and given by one-dimensional averages taken from the simulations. The standard Haan prescription [16] is used to handle weak nonlinear behavior. The predicted imprint is shown as the flat first section of the curve; it ends at 4 nsec. The imprint level matches the maximum of the simulated mode amplitude between 2 and 4 ns quite well, which shows that numerical mode coupling in the linear growth phase is not an issue. After the imprint, the predictions and simulations separate. In almost every case, the growth seen in the simulation lags that in the simple formula. This time lag, which varies from 1-2 ns and occurs as the laser pulse is increasing rapidly, corresponds to the period during which the outer ablation surface is being accelerated at a higher rate than the target inner edge. The target compression is time-dependent and nonuniform, and the RT dispersion relations (derived under more ideal conditions) do not satisfactorily describe the evolution during this time. In all wavelengths simulated, the growth during this stage is less than the RT predictions. Similar results are seen for the optically smoothed driven

target, the only difference being that the imprint level is less accurate due to the statistical laser realization in this particular simulation.

The failure of the model at the beginning of the RT growth phase is not due to the particular dispersion relation chosen. We have also tried the simpler Bodner-Takabe relation [1,2] ($\gamma = 0.9\sqrt{kg} - 3kV_a$) as well as the more complex formula developed by Sanz and Betti in the large Froude number limit [13,4], and there is very little difference in the predicted growth for this target. In addition, the use of areal mass instead of surface perturbation amplitude as a point of comparison does not contribute to this mismatch, but instead decreases it. The outer surface density increases along with the acceleration, which can lead to a corresponding increase in the areal mass perturbation even without a concomitant increase in the surface amplitude.

Finally, we turn our attention to the original problem that began this study, the spherical all-DT NIF target (Fig. 1). We performed a simulation of this pellet using both a 500Å surface finish and a 1 THz optically smoothed laser consisting of 32 polarization-smoothed overlapped beams focused onto the pellet with f/30 optics and a spot size equal to the initial pellet diameter. The simulation section was the width of an $\ell=12$ mode and used 256 points in the transverse direction, so that modes from $\ell=12$ to $\ell=192$ were resolved with at least 16 points per mode. The transverse boundary conditions were periodic, and a wavenumber-averaged 2D optically-smoothed spectrum was used that preserves the total rms fluctuation level of the intensity spectrum:

$$\langle I(\kappa) \rangle = \sqrt{\kappa \left(\pi - 2 \sin^{-1} [\kappa] - 2\kappa\sqrt{1 - \kappa^2} \right)} \sqrt{\frac{\pi}{4N_z}} I_{avg} \quad (7)$$

In contrast to the line-out spectra represented by Eqs. (2) or (3) which peak as $\kappa \rightarrow 0$, this averaged spectrum peaks at $\kappa \simeq 0.4$, or $\ell \simeq 400$ thus giving more weight to the smaller wavelength intensity perturbations. Pellet density images during the compression and implosion, along with a plot of $\sigma_{rms}(t)$ from the simulation are shown in Fig. 9. The simple model predictions are also shown on the same graph. As in the planar targets, the predictions match the level of imprint in the foot and the growth rate during the high power

part of the pulse, but again a delay time is seen between the growth predicted by the simple models and the growth seen in the simulation. The saturation of the predicted growth occurs at about 7 nsec, midway through the drive pulse, while the simulation shows a later and more extended period of growth, with the maximum areal rho-dr occurring at stagnation. (Although the areal mass perturbation in the simulation becomes larger than the total original areal mass, the shell does not completely break up because convergence has greatly increased the total shell rho-r at this time. The maximum simulation amplitude is about 20% of the total rho-r, occurring at about 8.2 nsec.) Due to convergence and nonlinearity, we do not expect the quasilinear modifications to the predicted growth to remain accurate.

We strongly urge caution when extrapolating these simulation results to expectations of the actual 3D evolution behavior of a real DT pellet. As the spectrum of target modes is limited to 1D transverse variations, the resulting mode amplitude in any single mode is significantly larger here than on an actual pellet. While linear growth rates should be the same as in the 3D case, the absolute mode amplitude and nonlinear interactions cannot properly be taken into account in 2D.

The real test of the simulation code, and the final arbiter of truth, is in comparison with experiment. As a recent example of the ability of our code to simulate measurable real-world quantities accurately, we show a comparison of the code results to a series of experiments that used the Nike KrF laser to accelerate a $150\mu\text{m}$ thick target composed of a low density resorcinol formaldehyde foam (50 mg/cc) into which liquid Deuterium was wicked. The target was coated by a $2\mu\text{m}$ thick layer of Kapton onto which a $60\mu\text{m}$ wavelength, 1D 1000\AA deep sine-wave ripple was imposed. It was accelerated by a two-step 1-THz pulse from the Nike laser, composed of a 4 ns main pulse at about $8 \times 10^{13}\text{W}/\text{cm}^2$ preceded by a ~ 4 ns foot at about 5% of the main intensity. X-ray framing cameras recorded emission from a backlighter that was created by illuminating a Mg sample with 12 Nike beams [17]. The backlighter emission passes through the target and is reflected and focused by curved crystal imagers that pass only a small band ($\sim 10\text{eV}$) of x-rays near the 1.45 KeV Mg line back to the cameras [18]. The target images are recorded at different times during the target

acceleration, and are analyzed using the known material opacity to determine the areal mass nonuniformity. These results are plotted in figure 10. Simulation of this experiment using the FAST2D hydrocode produced the solid curve shown in the figure. The simulation results match well, and are within the experimental error bars.

V. CONCLUSIONS

We have compared single and multimode simulations to simple Richtmyer-Meshkov and Rayleigh-Taylor theoretical models. The Richtmyer-Meshkov sharp boundary model is used for early times to compare to surface perturbation and stationary intensity imprint evolution. Rayleigh-Taylor dispersion relations are used as the intensity increases and the ablation surface is accelerated. We have applied these models to predict the instability evolution in an all-DT direct drive ICF target.

The simulations of Richtmyer-Meshkov exhibit similarities and differences compared to the theoretical predictions. In general, the simulation and theory agree that the largest RM response occurs for perturbation wavelengths near $100 \mu\text{m}$. For the case of surface perturbation seeded RM, the simulations show a larger response for shorter wavelengths ($\lambda < 100\mu\text{m}$) compared to the model. In this same regime, the SBM predicts a growth factor that is relatively independent of wavelength (Fig. 3). At the larger wavelengths, the responses are comparable and decrease as the wavelength increases. Evolution details like the initial phase reversal time for the mode and the subsequent oscillatory behavior can be different in detail but are similar in general.

For the case of stationary intensity-driven RM perturbations (imprint), the simulations tend to show earlier saturation behavior and smaller amplitudes than the model at the shorter perturbation wavelengths ($\lambda < 70\mu\text{m}$). At larger wavelengths ($\lambda > 200\mu\text{m}$) simulation and theory give a similar response. The largest discrepancy appears in the peak range $\lambda \sim 70 - 200\mu\text{m}$, where the simulations show a larger imprint response (Fig. 4). The simulated RM response is thus more peaked than the theoretical predictions. Imprint of

optically smoothed lasers is also simulated and its imprint efficiency is found (Fig. 5) to be peaked in the same $100\mu\text{m}$ range as the stationary imprint. Comparison of these results to the stationary intensity imprint also yields an implied smoothing time that varies in the range of 0.1-1.0 nsec.

Finally, the computed growth factors and imprint efficiency from the RM phase are used with the dispersion relations of several RT models to predict the total instability growth throughout the target compression and acceleration. We find that this type of simple modeling overestimates growth compared to simulations. The main cause of this overestimation is the failure of the models to adequately describe the transition between RM & RT. Using the RT model to describe the instability evolution at the accelerating ablation surface at this time leads to larger perturbation growth than seen in the simulations. During this transition, the laser intensity is constantly increasing, target compression is variable, and neither the RM model nor the current RT theory is strictly applicable. Potentially, a better ansatz could be developed than was used here, which could perhaps yield a better predictive capability with these existing models. However, we believe that the results here illustrate that separate analysis of this transition phase may be a fruitful area for future theoretical attention.

VI. ACKNOWLEDGMENTS

The authors would like to acknowledge useful discussions with Dr. S. Bodner. Drs. Marcel Klapisch and Denis Colombant supplied the STA opacities used in the FAST2D code. We would also like to thank the (anonymous) referee for useful and helpful comments about the manuscript. This work was supported by the U.S. Department of Energy.

REFERENCES

- [1] S.E. Bodner, Phys. Rev. Lett. **33**, 761 (1974).
- [2] H. Takabe, K. Mima, L. Montierth, and R. L. Morse, Phys. Fluids **28**, 3676 (1985).
- [3] S.W. Weber, S. G. Glendinning, D. H. Kalantar, *et al.*, Phys. Plasmas **5**, 1989 (1997).
- [4] R. Betti, V.N. Goncharov, R.L. McCrory, and C. Verdon, Phys. Plasmas **5**, 1446 (1998).
- [5] R. Ishizaki and K. Nishihara, Phys. Rev. Lett. **78**, 1920 (1997); R. Ishizaki and K. Nishihara, Phys. Rev. E **58**, 3744 (1998).
- [6] R.J. Taylor, A.L. Velikovich, J.P. Dahlburg, and J.H. Gardner, Phys. Rev. Lett. **79**, 1861 (1997).
- [7] A.L. Velikovich, J.P. Dahlburg, J.H. Gardner, and R.J. Taylor, Phys. Plasmas **5**, 1491 (1998).
- [8] V.N. Goncharov, Phys. Rev. Lett. **82**, 2091 (1999); V. Goncharov, S. Skupsky, T. Boehly, *et al.*, Phys. Plasmas **7**, 2062 (2000).
- [9] A.L. Velikovich, J.P. Dahlburg, A.J. Schmitt, *et al.*, Phys. Plasmas **7**, 1662 (2000).
- [10] J.H. Gardner, A.J. Schmitt, J.P. Dahlburg, *et al.*, Phys. Plasmas **5**, 1935 (1998).
- [11] A.L. Velikovich, A.J. Schmitt, J. H. Gardner, and N. Metzler, Phys. Plasmas **8**, 592 (2001).
- [12] S.E. Bodner, D.G. Colombant, J.H. Gardner, *et al.*, Phys. Plasmas **5**, 1901 (1998).
- [13] J. Sanz, Phys. Rev. Lett. **73**, 2700 (1994); J. Sanz, Phys. Rev. E **53**, 4026 (1996); A.R. Piriz, J. Sanz, L.F. Ibañez, Phys. Plasmas **4**, 1117 (1997).
- [14] See EPAPS Document No. E-PHPAEN-8-992105 for “Analysis of intensity structure of the ISI model in the FAST2D hydrocode” by A.J. Schmitt. This document may be retrieved via the EPAPS homepage (<http://www.aip.org/pubservs/epaps.html>) or from

ftp.aip.org in the directory /epaps/. See the EPAPS homepage for more information.

- [15] R. Betti, V. Lobatchev, and R.L. McCrory, Phys. Rev. Lett. **81**, 5560 (1998).
- [16] S.W. Haan, Phys. Rev. A **39**, 5812 (1989).
- [17] C.J. Pawley, S.E. Bodner, J.P. Dahlburg, *et al.*, Phys. Plasmas **6**, 565 (1999).
- [18] Y. Aglitskiy, T. Lehecka, S.P. Obenschain, *et al.*, Rev.Sci.Instrum. **70**, 530 (1999).

FIGURES

FIG. 1. An all-DT direct drive pellet similar to that planned for the National Ignition Facility (NIF). The Richtmyer-Meshkov growth phase lasts until about 4 nsec, when the laser pulse begins to increase. Shock breakout from the inner target surface occurs at about 5.8 nsec.

FIG. 2. Comparison of theoretical and simulated surface perturbation growth as a function of time for a variety of perturbation wavelengths. The black line indicates simulation results, the gray is the simple model.

FIG. 3. Growth factor of surface perturbations. The black line is from simulation results, the gray from the model.

FIG. 4. (a) Comparison of imprint and theory vs time for different wavelengths; (b) The imprint efficiency of stationary intensity perturbations. The black line indicates simulation results, the gray is the simple model.

FIG. 5. (a) Imprint vs wavelength for optically smoothed light. (b) Imprint efficiency for optical smoothing vs wavelength.

FIG. 6. The implied smoothing time found by comparing optically smoothed imprint to stationary imprint.

FIG. 7. The feedout growth factor (Eq. 5 in the text.) is worst at the wavelength $\lambda = L_0/6$, for targets of original thickness L_0 .

FIG. 8. Comparison of individual mode growth for nonuniform surface finish (top five plots) and of optically-smoothed driven imprint (bottom five plots). The black line indicates simulation results, the gray is the simple model.

FIG. 9. (a) Images of shell density at six different times during the implosion; (b) comparison of σ_{rms} vs. time for the simulation (black curve) and the predictions using imprint model plus Weber RT growth formula (dash-dotted), Bodner-Takabe formula (gray), and Sanz-Betti formula (dash).

FIG. 10. Experimental results (square cross icons) of surface perturbation growth compared to the FAST2D hydrocode simulation.

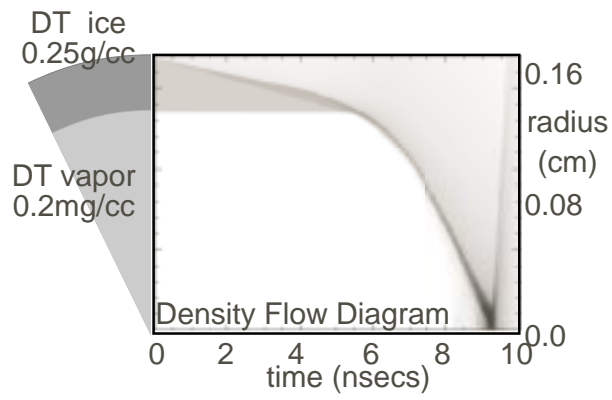
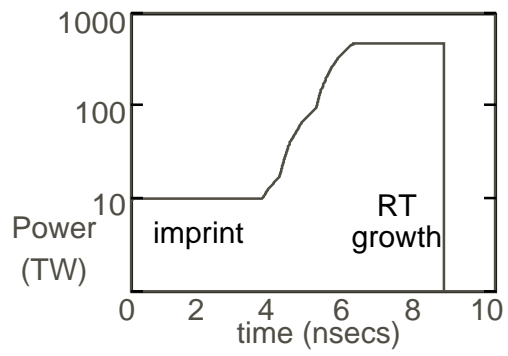


Fig. 1

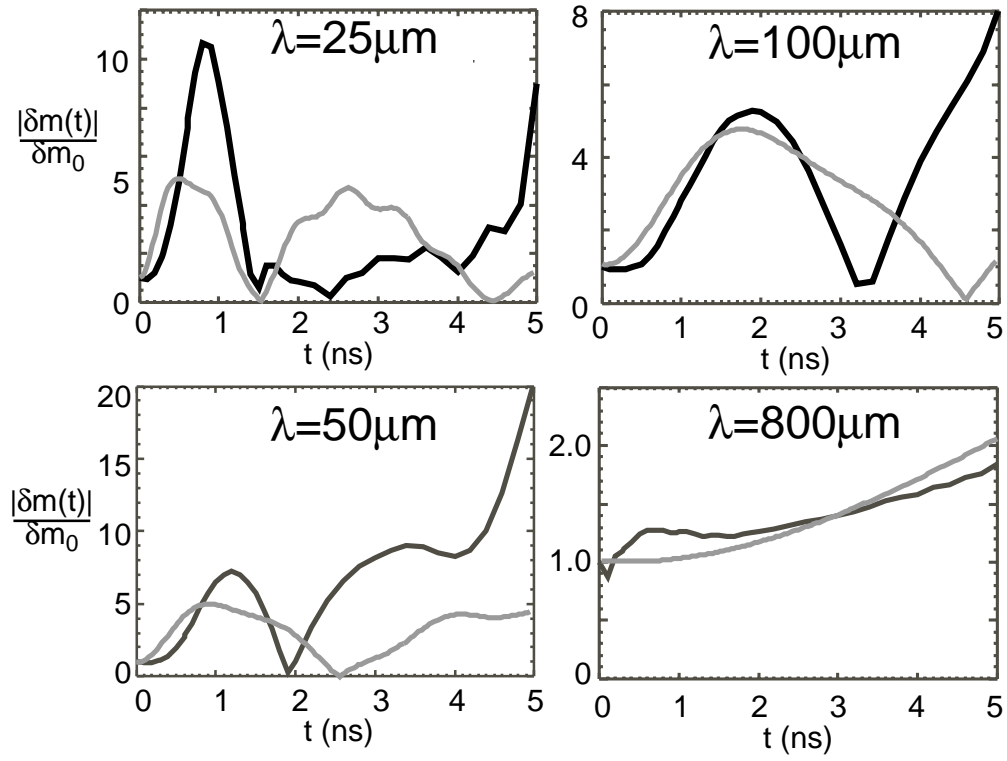


Fig. 2

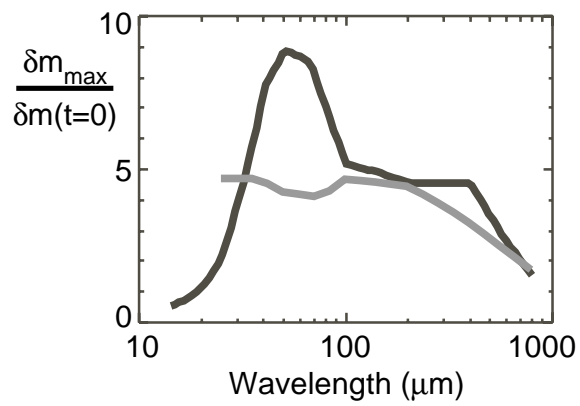


Fig. 3

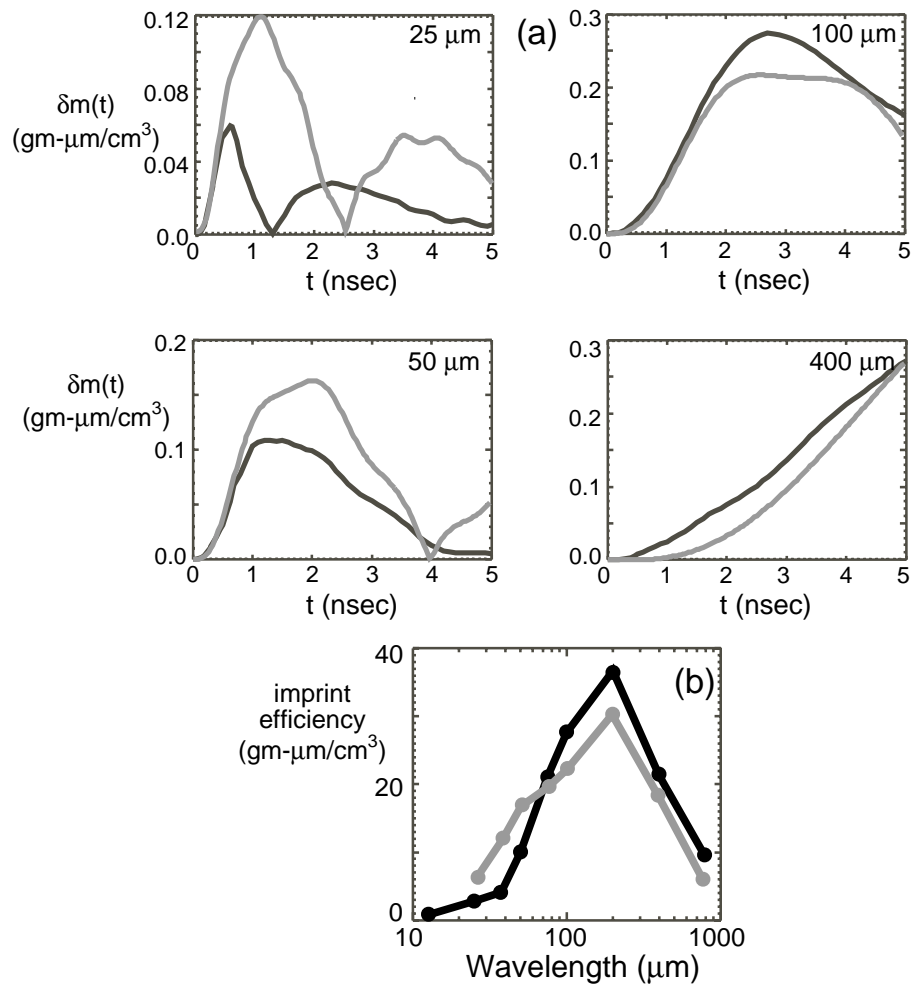


Fig.4

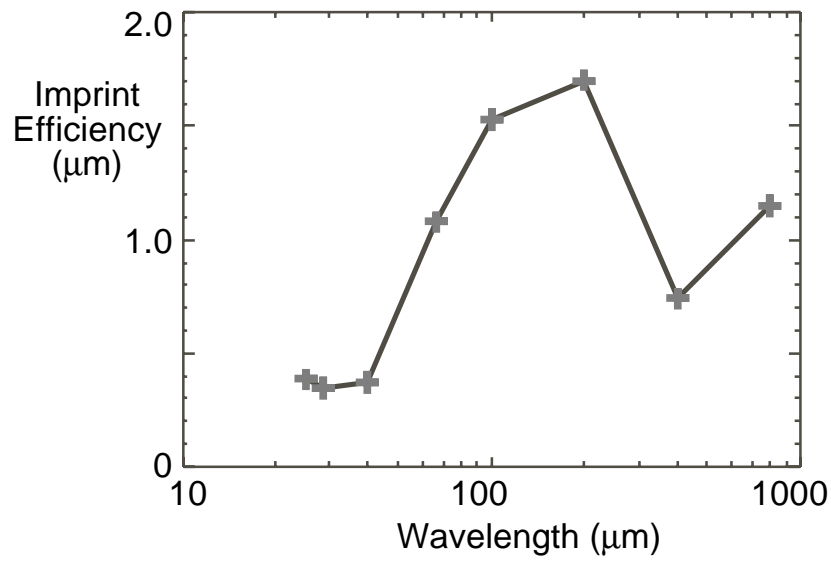
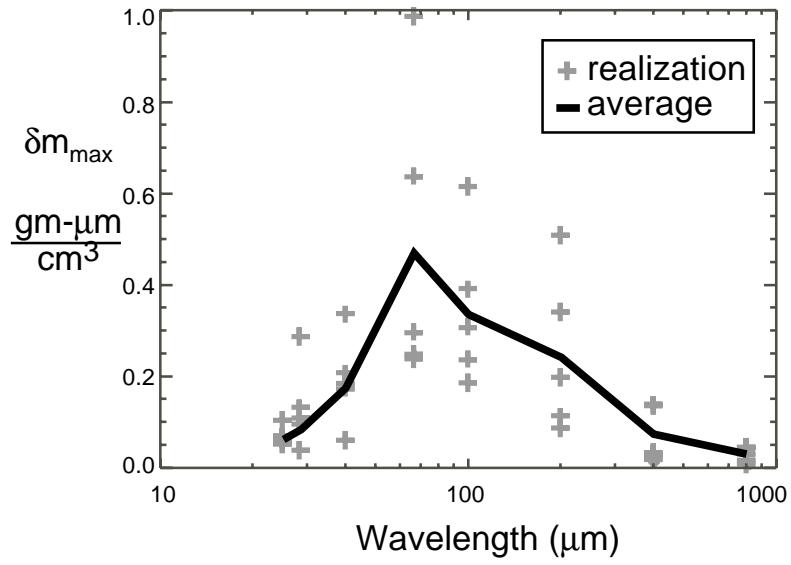


Fig. 5

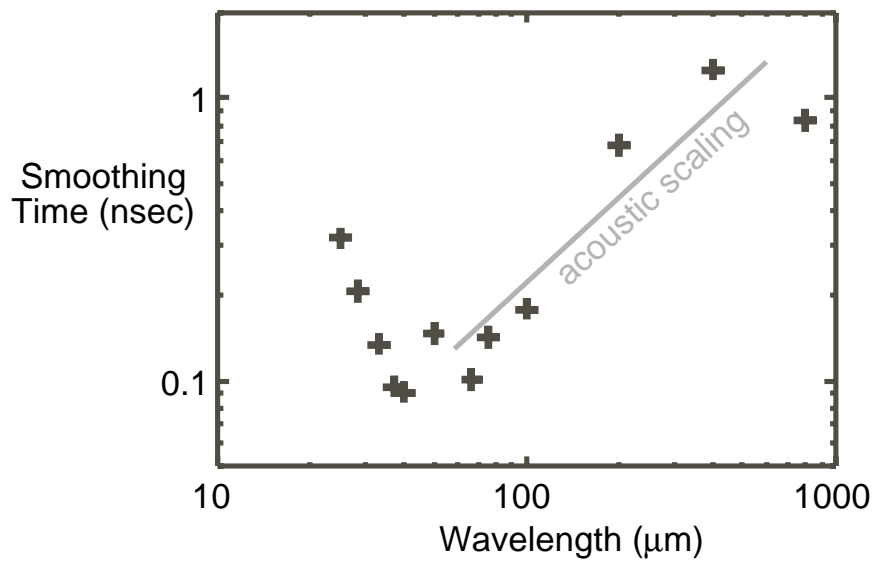


Fig. 6

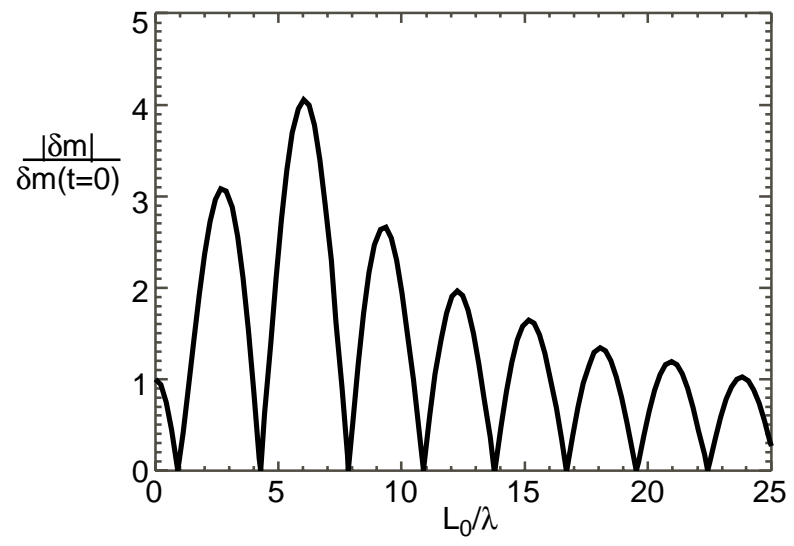


Fig.7

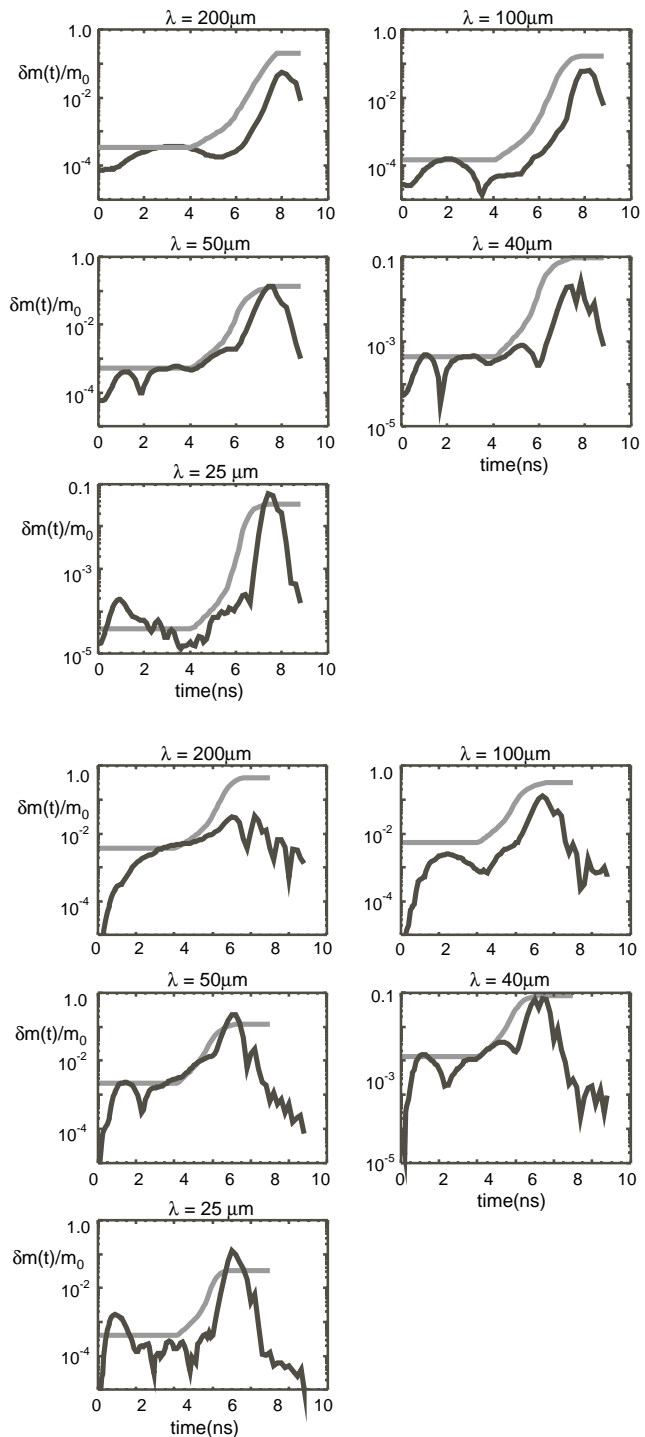


Fig. 8

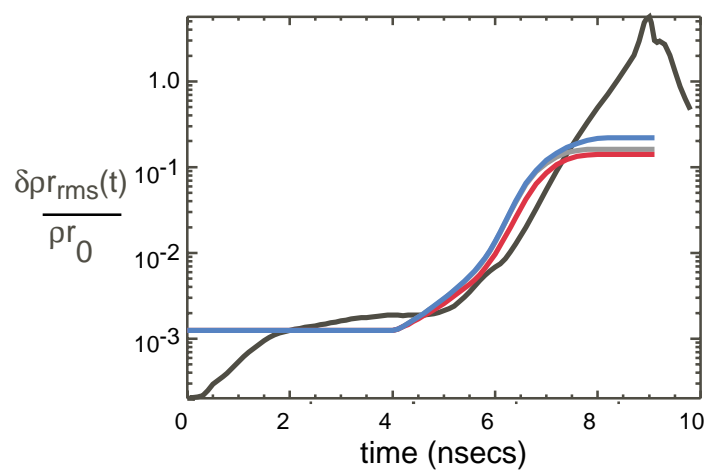
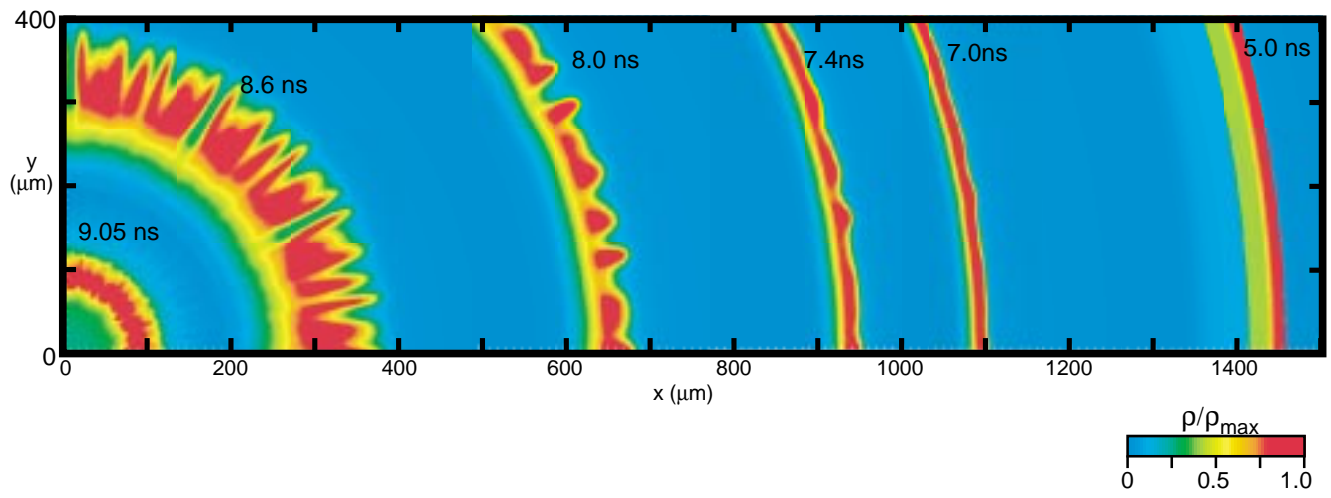


Fig. 9

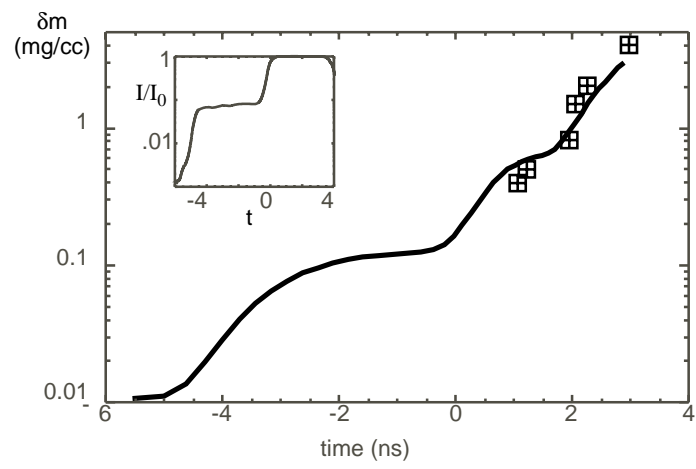


Fig.10